



This is a repository copy of *Innovative blade-structured rotor design for enhanced self-cooling in permanent magnet machines*.

White Rose Research Online URL for this paper:

<https://eprints.whiterose.ac.uk/id/eprint/231087/>

Version: Published Version

---

**Article:**

Li, K.L. and Li, G.-J. orcid.org/0000-0002-5956-4033 (2025) Innovative blade-structured rotor design for enhanced self-cooling in permanent magnet machines. IET Electric Power Applications, 19 (1). e70088. ISSN: 1751-8660

<https://doi.org/10.1049/elp2.70088>

---

**Reuse**

This article is distributed under the terms of the Creative Commons Attribution (CC BY) licence. This licence allows you to distribute, remix, tweak, and build upon the work, even commercially, as long as you credit the authors for the original work. More information and the full terms of the licence here:

<https://creativecommons.org/licenses/>

**Takedown**


If you consider content in White Rose Research Online to be in breach of UK law, please notify us by emailing [eprints@whiterose.ac.uk](mailto:eprints@whiterose.ac.uk) including the URL of the record and the reason for the withdrawal request.



[eprints@whiterose.ac.uk](mailto:eprints@whiterose.ac.uk)  
<https://eprints.whiterose.ac.uk/>

## ORIGINAL RESEARCH OPEN ACCESS

# Innovative Blade-Structured Rotor Design for Enhanced Self-Cooling in Permanent Magnet Machines

Kaile Li | Guang-Jin Li 

School of Electrical and Electronic Engineering, University of Sheffield, Sheffield, UK

**Correspondence:** Guang-Jin Li ([g.li@sheffield.ac.uk](mailto:g.li@sheffield.ac.uk))

**Received:** 15 April 2025 | **Revised:** 17 July 2025 | **Accepted:** 3 August 2025

**Handling Editor:** Yacine Amara

**Funding:** The authors received no specific funding for this work.

**Keywords:** AC machines | computational fluid dynamics | permanent magnet machines | thermal analysis

## ABSTRACT

This paper proposes a novel self-cooling solution for surface-mounted permanent magnet machines, which are widely used in various industry sectors. By properly designing a propeller and integrating it into the rotor structure, leading to a blade-structured rotor design, the self-cooling capability is achieved without the need for rotor wafters or rotor mounted fans. When rotor rotates, the cooling air (coolant) is drawn into the machine through inlets and expelled from the outlets, both inlets and outlets can be in the endplates or in the housing. During this process, air will thoroughly contact various internal components, such as end-windings, stator and rotor iron cores, along its flow path. As a result, internally generated heat in the windings and in the rotor mounted permanent magnets will be removed effectively. The study focuses particularly on the hot spots (locations with highest temperature) along the airflow path, such as the end-windings and permanent magnets. Different factors that affect the efficacy of this self-cooling solution, such as the number of propeller blades, position and size of inlets and outlets and rotor rotational speeds, are studied and compared. These studies are initially based on 3-dimensional computational fluid dynamic models and later validated through a series of experiments.

## 1 | Introduction

Permanent magnet (PM) machines have become increasingly prevalent in industries, such as electrical and hybrid electrical vehicles, renewable energies and aerospace, due to their many advantages over conventional wound field and induction machines. For example, PM machines generally boast a simpler structure, smaller size, lighter weight and greater efficiency. However, PM machines experience various types of operational losses, including copper losses, iron losses, PM eddy current loss and mechanical losses. These losses are heat sources inside electrical machines that contribute to temperature rise within different machine components such as windings and PMs. This is particularly problematic for PMs as the rare earth materials

used in PMs are highly sensitive to temperature rise [1] and high-temperature environments can degrade their magnetic performance [2], thereby decreasing the machine's efficiency [3]. As a result, effective thermal management for high power density PM machines becomes critical for maintaining their optimal performance [4–6].

It is well-established that the most widely adopted cooling solutions in industry and academia are based on heat transfer through conduction and/or convection, as for the heat radiation to be effective, it requires large temperature gradient ( $> 100^{\circ}\text{C}$ ) that often does not exist inside electrical machines. There are two types of convection heat transfer modes, that is, natural convection and forced convection. To enhance the heat transfer

This is an open access article under the terms of the [Creative Commons Attribution](https://creativecommons.org/licenses/by/4.0/) License, which permits use, distribution and reproduction in any medium, provided the original work is properly cited.

© 2025 The Author(s). *IET Electric Power Applications* published by John Wiley & Sons Ltd on behalf of The Institution of Engineering and Technology.

by natural convection, housings with additional fins are employed to increase the interaction between the machine and the surrounding air [7]. Potting materials are inserted into the gap between the housing and stator to improve thermal conductivity [8]. Similarly, heat pipes are embedded in the slots to facilitate heat dissipation from the windings to the exterior [9].

In addition to natural cooling methods, forced air or liquid cooling is also widely employed in industrial applications. This is because high power density working conditions, such as high rotation speeds, generate significant heat inside machines, necessitating the use of forced cooling techniques [10]. One effective forced cooling solution is the flooded or semiflooded stator, where the air inside the machine is replaced with fluid, which has a higher heat transfer coefficient (HTC) [11]. This approach allows heat to be dissipated more efficiently. Additionally, water jacket cooling is a widely used and highly effective method for dissipating heat by integrating it with the machine housing, particularly for removing the heat generated in the stator [12]. Another common forced cooling method involves mounting an additional fan onto the rotor shaft. As the rotor rotates, the fan generates an axial airflow, allowing cold air to circulate through the machine's interior [13]. This rotor mounted fan cooling is highly effective but requires additional space within the machine's structure to install the cooling fan [14]. For instance, using an extra fan for cooling necessitates dedicated areas on both sides of the shaft, increasing the overall axial length and hence the machine size [15, 16]. This is problematic in applications demanding high power (and torque) density, such as electric vehicles, where space is limited. Additionally, forced cooling can introduce extra losses. For example, a flooded stator system requires power to pump cold fluid in and out of the machine, causing frictional head losses [17]. Therefore, a forced cooling solution that minimises impact on power density while maintaining an acceptable loss level is needed [18].

To address the above challenges, a flux switching PM machines with self-cooling capability has been developed in Ref. [15], where extra fan blades are integrated into the rotor teeth, leading to aerofoil shaped rotor, which helps generate axial airflow as the rotor spins. For outer rotor PM machines, spiral grooves on the outer rotor's inner surface create axial airflow to dissipate heat [19]. However, these solutions are not applicable to surface-mounted permanent magnet (SPM) machines and interior permanent magnet (IPM) machines, which are two main machine topologies widely adopted in machine industry. The design of installing NASA-2412 aerofoil blade structures inside the rotor can achieve self-cooling capability. However, due to the limitations of the NASA-2412 aerofoil blade structure, such as small axial length, its applicability is not widespread and is not suitable for machines with a longer stack length [14]. This paper explores the possibility of integrating a propeller into the rotor iron core, essentially between the shaft and the rotor core, in order to achieve a SPM or IPM machine with self-cooling capability. For simplicity, only SPM machine has been chosen for proof of concept as shown in Figure 1. The internal structure of the propeller-like rotor draws in cold air through the inlets on the end-cap during rotation. The airflows through machine components such as the end-windings and the outer side of the permanent magnets, enters the interior of the rotor and is then

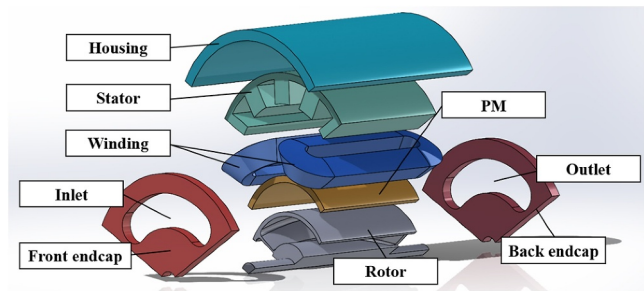


**FIGURE 1** | Exploded view of the SPM machine with blade rotor for self-cooling capability.

expelled through the outlets on the opposite end-cap. To investigate its cooling efficiency, numerous computational fluid dynamics (CFD) simulations will be conducted in this paper and the numerical results will be validated by experiments.

## 2 | CFD Modelling of Self-Cooling Machine

### 2.1 | CFD Modelling

In CFD simulations related to engineering airflow, one of the biggest challenges is turbulence, as the reliability of turbulence modelling directly affects the accuracy of CFD results, making it extremely important. Generally, there are three methods used for establishing turbulence models: direct numerical simulation (DNS), Reynolds-averaged Navier–Stokes equations (RANS) and large eddy simulation (LES) [20]. These methods are applied based on different requirements for degrees of freedom in the solutions, and their computational costs can be simply stated as  $LES < RANS < DNS$ . Since the fluid field within electrical machines is typically turbulent, the use of these models is unavoidable [21]. LES is widely used in simulating the fluid field of electrical machines due to its relatively short computation time. In addition to LES, this paper also employs a  $k-\omega$  turbulence model with a shear stress transport (SST) formulation, which directly acts on the wall surface of the model through the viscous sublayer. This reduces the model's sensitivity to free-stream turbulence at the inlet, thereby improving the model's stability [22].

In addition, in industrial CFD modelling, the moving reference frame (MRF) method is commonly used to model challenges involving rotating parts [23]. This method is efficient and requires relatively low computational power, making it suitable for most industrial applications. The MRF method is based on a straightforward and elegant principle: during the meshing phase, a small volume of grid cells is created around the rotating body, forming the MRF region. During the simulation phase, the MRF region rotates around the axis of the rotating body, whereas the body itself remains stationary. The governing equations are solved in a reference frame that moves at the same speed as the rotating geometry. Physically, this approach allows us to observe the flow field around the moving object as if we were situated on it, resulting in a stable flow field around the geometry [24]. These principles will be employed for the predictions of fluid behaviour of the proposed SPM machine with self-cooling capability in this paper and will be elaborated further in the following sections.

It is worth noting that the CFD models developed in this paper use cubic meshes with small volumes ( $< 0.5$  mm) to ensure the accuracy of the simulation results. Additionally, to save computation time, all models were built using a 1/3 scale, and rotational periodic boundary conditions are applied to simulate the operation of a full motor model. To enhance the sensitivity of components, such as the PM and end-winding to temperature changes in the air domain, additional inflation layers are created on their surfaces. These inflation layers are divided into seven layers, with the smallest mesh layer being 0.1 mm.

## 2.2 | Machine Structure and Material Properties

The SPM machine adopted in this paper can be seen in Figure 1. Its key specifications are listed in Table 1. The thermal characteristics of the machine components are shown in Table 2 and the coolant (air) characteristics are as follows: density is  $1.185 \text{ kg/m}^3$ , thermal conductivity is  $0.0261 \text{ W/m} \cdot \text{K}$ , dynamic viscosity is  $1.831 \times 10^{-5} \text{ Pa} \cdot \text{s}$  and specific heat capacity is  $1.004 \times 10^3 \text{ J/kg} \cdot \text{K}$ . It is worth noting that air is treated as an incompressible fluid in the simulations. To simplify the CFD modelling, thermally anisotropic materials were introduced in the coils to represent the mixture of copper and impregnation in the stator slots. The HASHIN approximation was used to calculate the anisotropic thermal conductivity of this material [25]. It was assumed that the slot filling factor was 0.4 for all the machines studied, and the conductivity perpendicular to the direction of the current was  $0.65 \text{ W/m} \cdot \text{K}$ , whereas the conductivity parallel to the direction of the current was  $160 \text{ W/m} \cdot \text{K}$ . The average density is  $4269 \text{ kg/m}^3$  and the average specific heat capacity is  $1174 \text{ J/kg} \cdot \text{K}$ .

**TABLE 1** | Parameters of SPM machine.

Slot number	12
Pole number	10
Stator outer radius (mm)	45
Rotor outer radius (mm)	26.5
Airgap length (mm)	1
Magnet thickness (mm)	3
Stack length (mm)	50
DC voltage (V)	72
Rated RMS current (A)	7.07
No of turns per coil	35
Rated speed (rpm)	3000

**TABLE 2** | Properties of machine solid components.

	Housing	Rotor/stator	Magnet	Shaft
$\rho$ ( $\text{kg/m}^3$ )	2790	7650	7500	7800
$\lambda$ ( $\text{W/m} \cdot \text{K}$ )	168	30	7.6	52
$c$ ( $\text{J/kg} \cdot \text{K}$ )	833	460	7500	460

Note:  $\rho$ ,  $\lambda$  and  $c$  denote the density, thermal conductivity and specific heat capacity, respectively.

Another important structural design aspect is the size and position of the inlets and outlets, which will determine the speed and direction of the inflow and outflow of the coolant (air), thereby affecting the cooling efficiency. This paper employs two different inlet/outlet designs, that is, axial inlet/outlet and radial inlet/outlet. As shown in Figure 2a, the axial design has the top edge 8 mm from the housing boundary and the bottom edge 30 mm from the shaft centre, positioned directly in front of the end-windings (EWs). As shown in Figure 2b, the radial design has the top edge 12 mm from the end-cap boundary and the bottom edge coinciding with the stator boundary positioned directly above the EWs. Both designs effectively allow sufficient contact between the air and the EWs, and the comparison of their impact on cooling efficiency will be discussed later in the paper.

In this paper, the structure of the rotor is one of the most important design factors. For rotors with integrated propellers to achieve self-cooling capability, the key design factors are the number of blades, their thickness and the span angle of each blade. In this paper, 5 different blade thicknesses ranging from 1 to 5 mm were studied and compared. In rotor structure, all blades are evenly distributed, with the total span angle not exceeding  $360^\circ$ . This is to ensure that the blades do not interfere with the airflow compressed by the other blades. As example, Figure 3 shows the rotor structures with 2–5 blades, other number of blades up to 7 will also be studied, as will be discussed later in the paper. All the blades used in this study are 2 mm thick and their height is 12.5 mm. It is also worth noting that as the primary focus of this paper is to demonstrate the effectiveness of the self-cooling concept, the blade shape was simplified and derived from a basic fan design commonly used in fan-like applications. Specifically, the blade geometry was

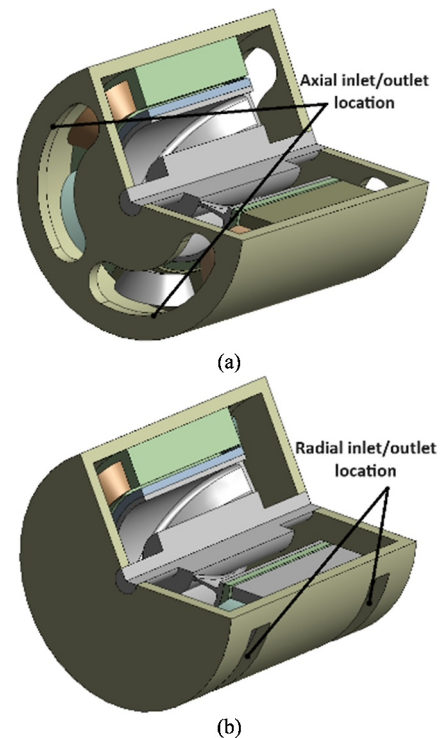


**FIGURE 2** | Locations of (a) axial inlet/outlet and (b) radial inlet/outlet.



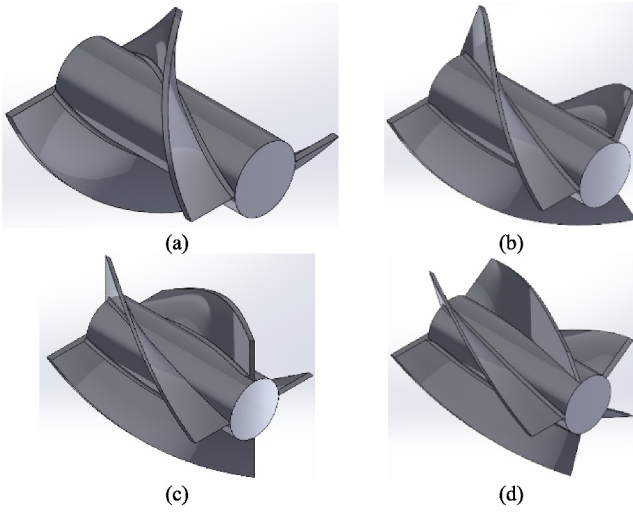


**FIGURE 3** | Rotor designs with different numbers of blades. (a) 2 blades, (b) 3 blades, (c) 4 blades and (d) 5 blades.

generated by sweeping a rectangular profile along a spiral path using SolidWorks 2023. Although more optimised and efficient blade designs could further enhance the cooling efficiency of the proposed system, these will be explored in future studies. In addition, the rotor can rotate in both clockwise and counter-clockwise directions with the same cooling efficiency.

Compared to traditional SPM machines, the addition of fan blades inside the rotor in this design may affect the mechanical stability of the machine at high speeds. Therefore, a study using ANSYS mechanical to analyse the deformation and surface pressure of blades with different thicknesses at varying rotational speeds has been conducted. The results have shown that, at speeds below  $10 \times 10^3$  rpm, the rotor radial deformation is in the nanometre range and the rotor surface pressure is well below the material's yield stress. As a result, it is concluded that the mechanical structure is stable at speeds under  $10 \times 10^3$  rpm.

### 2.3 | Windage Loss

Windage loss of a machine, also known as the wind erosion, refers to the power absorbed by the fluid surrounding the rotor due to the relative motion between the rotor and the stator [26]. As a result, the presence of windage losses deteriorates the efficiency of the machine since these losses cannot be converted into useful energy [27]. Another undesirable and sometimes the most important characteristic of wind erosion is that the absorbed energy is converted into heat, which raises the temperature of the rotor [28].

In this design, as the rotor draws air in and expels it while rotating, air drag will be produced on its surfaces, especially at the fan blade surfaces. This air drag generates additional heat in the rotor. In a typical SPM machine, it is challenging to cool the rotor mounted PMs as most of the heat (generated due to PM eddy current loss) conducts from rotor core to the shaft, which is not an effective heat removal path. In this case, the additional heat generated due to windage loss would make the PM cooling even harder. Consequently, the windage loss cannot be neglected in this

design. Accurately predicting the windage losses of the proposed machine is crucial for assessing its feasibility.

The prediction method for drag force is now very mature, with the drag coefficient being the most vital parameter. The drag coefficient is a number that aerodynamicists use to model complex dependencies of drag on shape, inclination and various flow conditions. This coefficient is derived from a rearrangement of the drag equation, solving for the drag coefficient in terms of the other variables. The drag coefficient  $C_d$  can be calculated as follows:

$$C_d = \frac{F_D}{\rho V^2 A / 2}, \quad (1)$$

where  $F_D$  is the drag force (N),  $\rho$  is density of air,  $V$  is the flow velocity (m/s) and  $A$  is the characteristic frontal area of the body ( $m^2$ ), referring to the area in the rotor, that is, perpendicular to the airflow.

The drag coefficient of different objects is mostly determined through experiments and is used to predict the drag force on common bodies. From Equation (1), it is found that the drag force depends on air velocity and the characteristic frontal area of body. Although the air drag force can also be obtained from Ansys CFX simulations, this prediction serves as a validation of the windage loss results from the simulations. Specifically, the windage loss was calculated and included as part of the total thermal load in our CFD model, ensuring its influence on local temperature fields is accurately represented.

### 2.4 | Boundary Conditions

The boundary conditions for the walls in the CFD model were all set to no-slip walls, meaning there is no slip between them (the relative velocity is 0 m/s). However, it is worth noting that the machine's housing and end-cap are connected to room temperature (25°C), so it is necessary to apply the heat transfer coefficient (HTC) to the outer wall surfaces. One of the most common ways to calculate the convective heat transfer coefficient is using the Nusselt number ( $Nu$ ), which is a dimensionless number that relates the convective to conductive heat transfer across a boundary. The general form of the equation is as follows:

$$h = \frac{Nu \cdot k}{L}, \quad (2)$$

where  $h$  is the convective heat transfer coefficient [ $W/(m^2 \cdot K)$ ],  $Nu$  is the Nusselt number (dimensionless),  $k$  is the thermal conductivity of the fluid [ $W/(m \cdot K)$ ] and  $L$  is the characteristic length (m).

The Nusselt number can be determined using empirical correlations that depend on the flow conditions. The flow type can be determined by calculating the Reynolds number:

$$Re = \frac{\rho v L}{\mu}, \quad (3)$$

where  $Re$  is Reynolds number (dimensionless),  $v$  is velocity of the fluid (m/s),  $L$  is characteristic length (m) (such as diameter in pipes or length in channels) and  $\mu$  is dynamic viscosity of the fluid (Pa·s).

Some common correlations between  $Nu$  and  $Re$  can be seen below [22].

$$Nu = \begin{cases} 0.664 \cdot Re^{\frac{1}{2}} \cdot Pr^{\frac{1}{3}}, & Re < 2000 \\ 0.037 \cdot Re^{0.8} \cdot Pr^{\frac{1}{3}}, & 2000 < Re < 4000, \\ 0.023 \cdot Re^{0.8} \cdot Pr^{0.3}, & Re > 4000 \end{cases} \quad (4)$$

with

$$Pr = \frac{C \cdot \mu}{k}, \quad (5)$$

where  $C$  is specific heat capacity at constant pressure [J/(kg·K)].

Through calculations, the HTC of the end-cap's outer wall is determined to be 10.7 W/(m<sup>2</sup>·K), whereas the HTC of the housing's outer wall is 12 W/(m<sup>2</sup>·K). Additionally, it is important to note that to better simulate the room temperature environment, an extra air domain was set up around the machine. The boundary conditions for this air domain were set to 25°C and six times the atmospheric pressure.

## 2.5 | Mesh Sensitive Test

It is well-established that the mesh quality is critical in CFD modelling. Generally speaking, smaller mesh size would improve the accuracy of the predictions. However, if the mesh size is too small, the simulation will be prohibitively computationally expensive. To achieve a good balance between the simulation time and accuracy, a mesh sensitive analysis has been conducted in this section. The impact of mesh size on the normalised temperature and normalised calculation time has been investigated as shown in Figure 4. It is worth noting that the air region is the most critical part for the CFD models, thus the analysis focuses on the mesh size within this region. The results indicate that reducing the average mesh size from 4 to 0.1 mm<sup>3</sup> (with the maximum mesh length decreasing from 5 to 1 mm) significantly increases the number of mesh elements by more than eight times and the computation time by approximately

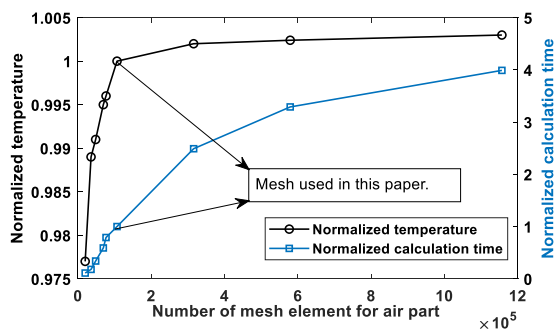


**FIGURE 4** | Normalised maximum temperature and calculation time at different number of mesh elements (and different mesh sizes).

3.9 times. However, the temperature variation is only 0.4%. Therefore, the mesh size selected in this study represents a reasonable compromise between model accuracy and computation time. As a result, a final decision has been made such that the machine's CFD model consists of 273,920 mesh elements and the number of mesh elements for air region is 106,869. The time step is variable, averaging around 1–2 s. The model is solved over 3000 iterations, requiring approximately 15 h on eight processors.

## 3 | Results and Discussion

Since forced air-cooling system is employed, the temperature-varying properties of air (especially density and dynamic viscosity) can be neglected. In addition, the compressibility of air is also negligible. A uniform fully developed airflow is introduced into the investigated machines with a mass flow rate of 0.48 kg/s and an inlet temperature of 25°C. For the forced cooling systems, the gravitational effect has been neglected. Therefore, the circumferential symmetry of the SPM machine leads to a circumferentially symmetric distribution of the flow field and heat transfer. In this case, a one-third (120°) segment is simulated for 3D CFD modelling. It is worth noting that the axial domain lengths both upstream and downstream of the machine are approximately 2 times and 3.5 times the machine length, respectively, to achieve a fully developed flow profile. This prevents the model from having unwanted 'backflow' that can cause poor convergence and inaccurate results.

As an example, Figure 5 shows the CFD simulation results of 3-blade rotor at a rotor speed of 3000 rpm. Since the flow rate is constant, a very high air velocity is reached due to the small

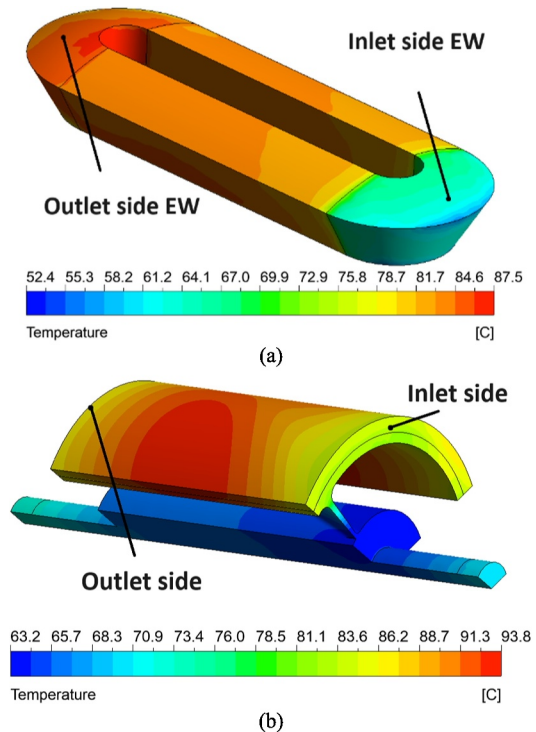


**FIGURE 5** | (a) Winding temperature distribution and (b) rotor temperature distribution of a 3-blades rotor.

inlet and outlet areas. The stator components benefit from the ventilated air, resulting in lower temperature, especially at the end-windings. For instance, as shown in Figure 5a, the inlet-facing part is more efficiently cooled, with a temperature of 52.4°C, whereas the outlet-facing part has the highest temperature, reaching 87.5°C. Moreover, the rotor component shows a slightly higher peak temperature, that is, 93.8°C as shown in Figure 5b. It is also found that the PM temperature decreases towards the blades, and the closer it is to the blades, the lower the temperature will be, with the lowest PM temperature being around 80°C. This is because the main heat-conducting path for PMs is from the blades to the shaft. In addition to this heat transfer through conduction, cold air from the inlet can also remove heat from the PM through forced convection. The presence of the blades increases the exchange surface area between the cold air and the rotor, acting as cooling fins and helping cool the PMs.

### 3.1 | Comparison Between the Self-Cooling Scheme With a Baseline External Fan-Cooled Machine

The baseline machine is shown in Figure 6; the model depicts the one-third representation of an external fan-cooled machine used for comparison with the self-cooling design proposed in this paper. To simulate the function of an external fan, the same pressure differential generated by the self-cooling rotor at the corresponding rotational speed is applied to the inlet and outlet located on the machine's end cap. For instance, at a rotational speed of 3000 rpm, the self-cooling design produces an approximate pressure difference of 20.3 Pa between the inlet and outlet. Accordingly, the inlet is set to a static pressure of 20.3 Pa, while the outlet is set to 0 Pa. This setup effectively mimics the airflow driven by a fan, blowing air from the inlet towards the outlet at a comparable velocity.

As a result, even though the inlet airflow velocity remains the same as in the self-cooling design, the overall cooling effectiveness differs due to the restricted airflow pathway.

As shown in Figure 7, the maximum PM and EW temperatures under both cooling strategies are plotted across various rotational speeds. It is evident that, at all speeds, the forced-air cooling system yields higher temperatures than the self-cooling system, and the temperature difference increases with speed. As the machine speed increases, the thermal performance gap between the self-cooling rotor design and the external fan-cooled system becomes more pronounced. This divergence is primarily due to

the limited airflow passage in the external fan-cooled configuration, in which the only path available for air to flow from the inlet to the outlet is through the narrow airgap. This restricts the effective utilization of increasing airflow at higher speeds. In contrast, the integrated self-cooling structure not only enables more direct and efficient airflow pathways (through the integrated fan blades) but also incorporates fan blades that enhance local heat dissipation, especially from critical components such as the PMs and EWs. Consequently, with higher speeds and greater heat generation, the self-cooling scheme scales more effectively, whereas the external fan-cooled system becomes increasingly constrained by its structural limitations.

### 3.2 | Influence of the Rotor Blade Dimensions

The CFD simulations have shown that varying the blade thickness did not lead to a significant improvement in cooling performance. For example, when using blades with a thickness of 2 mm, the maximum PM and EW temperatures were 93.8°C and 87.5°C, respectively. Increasing the thickness to 3–5 mm only caused a slight temperature variation of around 2°C. This is because, for fan-blade structures, increasing blade thickness does not significantly change the airflow rate, but it does increase blade weight and mechanical load. A 1 mm thickness was considered structurally insufficient due to potential mechanical weakness. Therefore, a 2 mm blade thickness was ultimately selected as the most appropriate compromise in this study.

However, it is found that the blade height has a pronounced impact on the self-cooling performance. As illustrated in Figure 8, the definition of rotor height refers to the radial dimension of the blade, with the rotor's inner surface at the PM

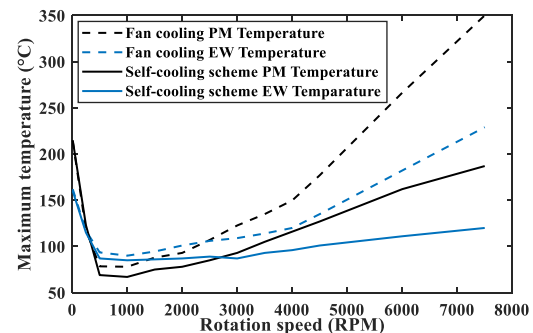


**FIGURE 7** | Maximum PM and EW temperatures comparison between the proposed self-cooling scheme and the baseline fan-cooled cooling scheme.

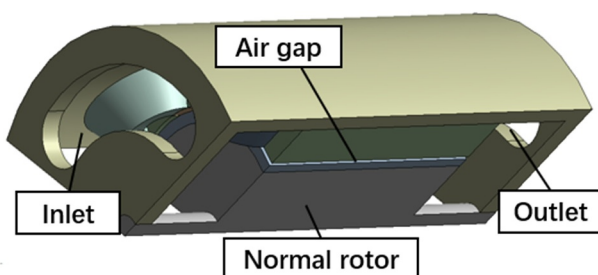


**FIGURE 6** | 1/3 model of the baseline external fan-cooled machine.

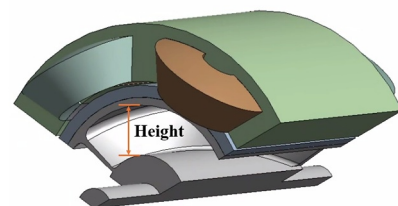


**FIGURE 8** | Height of the rotor blade.

remaining unchanged. Increasing the blade height effectively reduces the solid portion of the rotor and enlarges the volume available for airflow. As shown in Figure 9, the maximum PM temperature initially decreases and then slightly increases with blade height. At 0 mm height (i.e., a conventional solid rotor), the maximum PM temperature is 150.9°C. As the height increases to 10.5 mm, the temperature rapidly drops to 93.65°C, and with further increases up to 18 mm (where the blades directly connect to the shaft), it gradually rises to 99.3°C. For the EW, the maximum temperature continuously decreases with increasing height, dropping from 123.3°C at 0 mm to 86.5°C at 18 mm. This trend is due to the fact that with small blade height, the solid core portion of the rotor blocks the airflow path, reducing flow rate and heat transfer. As the blade height increases, this obstruction lessens, allowing better airflow and enhanced cooling. However, beyond a certain height (e.g., 15 mm), further increases primarily affect the root region of the blade and do not significantly enhance airflow. Moreover, taller blades may reduce the direct contact area between the cold air and the PM-facing rotor wall, which can slightly worsen PM cooling beyond this height.

Therefore, in this paper, a blade height of 12 mm was selected as an optimal balance, effectively enhancing the cooling of both the PM and EW regions under the self-cooling configuration.

### 3.3 | Influence of Different Numbers of Blades

Blades serve a dual function in the self-cooling machines, acting both as fan blades to generate airflow and as heat conduction paths between the PM and the shaft. When blade number changes, the cooling efficiency for EW and PM will be changed. Figure 10 shows the relationship between the number of blades, maximum PM and EW temperatures and axial airflow rate. It is found that, when the number of blades increases, the maximum PM temperature decreases continuously from 111.5°C to 87.5°C. The most significant drop occurs when the number of blades increases from 1 to 2, followed by a slower decline as more blades are added. The EW temperature initially decreases as the number of blades increases from 1 to 3, dropping from around 103°C–87°C. After this minimum, the temperature rises again, peaking at 111°C with 7 blades.

The axial airflow rate behaves very much opposite to the EW temperature. For instance, it first increases, reaching a peak of nearly 86 L/min when the number of blades is 2 or 3, and then

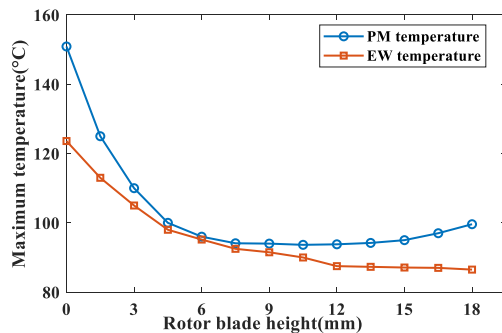


FIGURE 9 | PM and EW temperatures versus rotor blade height.

decreases steadily. For example, with 5 blades, the airflow rate drops to 54.7 L/min, which is lower than the 66.6 L/min observed with 4 blades. However, despite the reduced airflow, the cooling effect remains stronger with 5 blades for the PM temperature due to the increased surface area in contact with the air (8689.5 mm<sup>2</sup> compared to 6952.4 mm<sup>2</sup> for the 4-blade design as shown in Table 3). This increase in surface area enhances the heat removal capability, contributing to lower PM temperatures.

Considering both the PM and EW temperature trends, the optimal number of blades for this design is 3 or 4. However, since adding more blades increases windage losses in a fan-like structure, the final design uses 3 blades. This choice balances cooling efficiency and minimises losses, ensuring optimal temperature reduction while maintaining efficient airflow dynamics, leading to improved overall cooling performance.

### 3.4 | Influence of Different Rotor Speeds

In addition to the number of blades, the rotor speed is also an important factor that determines the cooling capability of the proposed design in this paper. In theory, increasing rotor speed will increase the airflow rate, leading to enhanced self-cooling capability. However, it also leads to increased losses, such as stator and rotor core losses, PM eddy current losses and windage loss within the electrical machines [29]. These losses are heat sources inside electrical machines and will contribute to machine temperature rise. As a result, when increasing the rotor speed to enhance self-cooling capability, special attention must be paid to the potential impact on temperature variation of the various machine components [30].

The total losses in a PM machine can be approximated by summing up the individual losses, that is, copper loss— $P_{cu}$ , core losses— $P_{core}$ , PM eddy current loss— $P_{eddy}$  and windage losses— $P_{mech}$ , such as

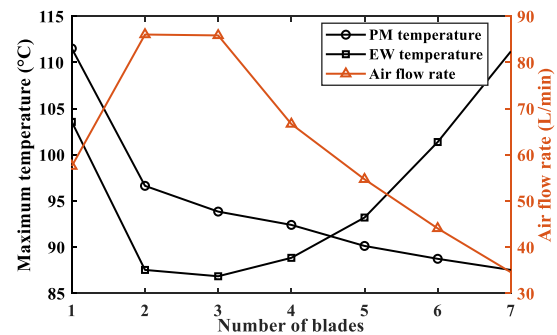


FIGURE 10 | Peak PM and EW temperatures and axial airflow versus blade number.

TABLE 3 | Angle per blade and total blade surface area.

	2-blade	3-blade	4-blade	5-blade
Blade span angle (°)	180	120	90	72
Surface area (mm <sup>2</sup> )	3758.6	4810.9	6952.4	8689.5



$$P_{\text{total}} = P_{\text{cu}} + P_{\text{core}} + P_{\text{eddy-mag}} + P_{\text{mech}}, \quad (6)$$

with

$$\begin{cases} P_{\text{cu}} = 3RI^2 \\ P_{\text{core}} = K_h B^2 f + K_c (Bf)^2 + K_e (Bf)^{3/2} \\ P_{\text{eddy}} = k_m (B_m f d)^2 \\ P_{\text{mech}} = k_{\text{mech}} \cdot \omega^2 \end{cases}, \quad (7)$$

where  $I$  is the phase rms current and  $R$  is the phase resistance;  $K_h$ ,  $K_c$  and  $K_e$  are the coefficients of hysteresis loss, classical eddy current loss and excess eddy current loss, respectively, and  $B$  is the peak flux density and  $f$  is the frequency;  $k_m$  is a constant related to the material properties and geometry and  $d$  is the PM thickness;  $k_{\text{mech}}$  is a mechanical loss constant and  $\omega$  is the angular velocity.

The calculated losses versus motor speed are shown in Figure 11. As for windage loss, at low speeds ( $< 4000$  rpm), it is very small ( $< 1$  W) compared to the PM eddy current loss and stator and rotor core loss. However, as the motor speed increases, the windage loss increases.

As mentioned above, increasing rotor speed can increase the rotor generated wind speed. However, in practice, this relationship is influenced by several factors, including but not limited to the shape and size of the fan blades, the air resistance and the turbulence [29, 31]. In this paper, a simplified empirical formula is used to estimate the relationship between rotor speed and the wind speed

$$V_f = K\omega D, \quad (8)$$

where  $V_f$  is the wind speed,  $K$  is the constant related to shape of the fan blades and the efficiency of the fan and  $D$  is the diameter of the fan blades.

Moreover, the flow rate created by the rotor rotation is

$$m_f = \frac{\pi D^2}{4} V_f. \quad (9)$$

Figure 12 shows the flow rates in the machine against the rotor rotation speed calculated by using Equation (9) and CFD modelling. Both results match well, and as expected, when rotor speed increases, the flow rate increases.

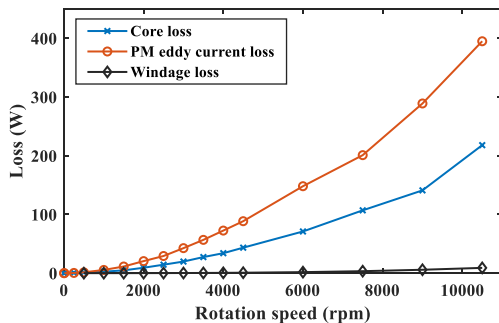


**FIGURE 11** | Various losses versus rotor speed.

In addition, as mentioned previously, a 3-blade design has been used for the investigations, so the constants, such as  $K$  and  $D$ , can be achieved, that is,  $K$  is 0.007 and  $D$  is 0.049 m. As a result, the relationship between the rate of heat transfer and the mass flow rates can be established such as

$$Q = \dot{m} \cdot C_p \cdot \Delta T, \quad (10)$$

where  $Q$  is the rate of heat transfer and  $\dot{m}$  is the mass flow rate of the air, which is  $m_f \times \rho$ , where  $\rho$  is the air density.  $C_p$  is the specific heat capacity of the air and  $\Delta T$  is the temperature difference between the incoming cold air and the machine being cooled.

Figure 13 illustrates the relationship between rotation speed and the maximum temperatures of PM and EW. For PM maximum temperature, it starts from high (215.3°C) at low rotation speed. Then, as the rotation speed increases, the temperature drops sharply, reaching its lowest value at around 2000 rpm. After that, the temperature rises with increasing rotation speed, reaching 286.3°C at 10,500 rpm. The EW maximum temperature shows the same trend as the PM, it is 158.4°C at low rotation speed, then it drops rapidly, reaching its minimum (approximately 60°C) at around 2000 rpm. The temperature gradually increases with the rotation speed, reaching about 150°C at 10,500 rpm. It is noted that, for both PM and EW, the best cooling effect happens within the range between 500 and 2000 rpm, where the fan blade can generate sufficient airflow with relatively low losses in the PM and EW. In the high-speed range, the losses generated exceed the cooling capacity of the

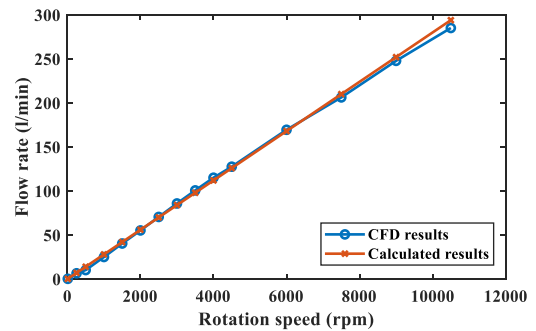


**FIGURE 12** | Flow rate against rotation speed calculated by CFD and Equation (9).

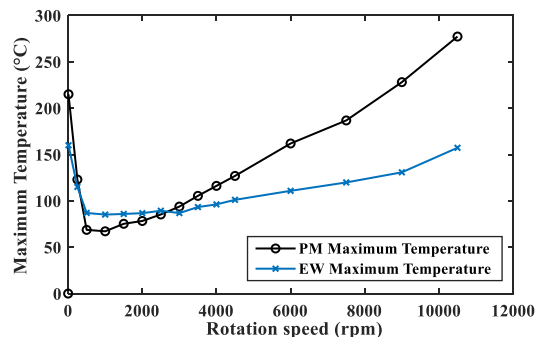


**FIGURE 13** | EW and PM peak temperatures versus rotor rotational speed.

fan-blade rotor, leading to elevated temperatures in both PM and EW.

Based on the above analyses, for the PM machines with self-cooling capability investigated in this paper, maintaining the speed below 4000 rpm (rated speed is 3000 rpm) achieves optimal cooling efficiency. At this speed, the temperatures of both the EW and PM can be maintained at relatively low levels, whereas the resulting windage loss remain minimal.

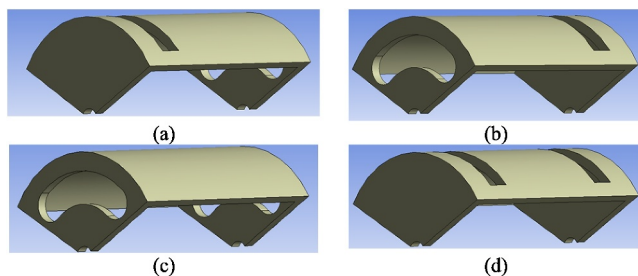
### 3.5 | Inlet and Outlet Locations

The design of the inlet and outlet is also critical for thermal management and overall cooling efficiency of the investigated machine with self-cooling capability. These inlets and outlets facilitate the flow of cooling air through the machine, ensuring that heat generated by the windings and PMs is effectively dissipated, thereby preventing overheating.

As mentioned previously, there are two main locations for placing the inlet and outlet, that is, axial design with inlet/outlet on the end-caps and radial design with inlet/outlet on the housing as shown in Figure 2. For all these designs, the inlets and outlets are directly facing the EW, minimising obstructions and maximising the cooling effect as cool air enters and hot air exits the machine. The shapes of these inlets and outlets are designed to enhance airflow through the EW, maximising the contact area between the cool air and the EW. Combining these configurations results in four different housing designs as shown in Figure 14.

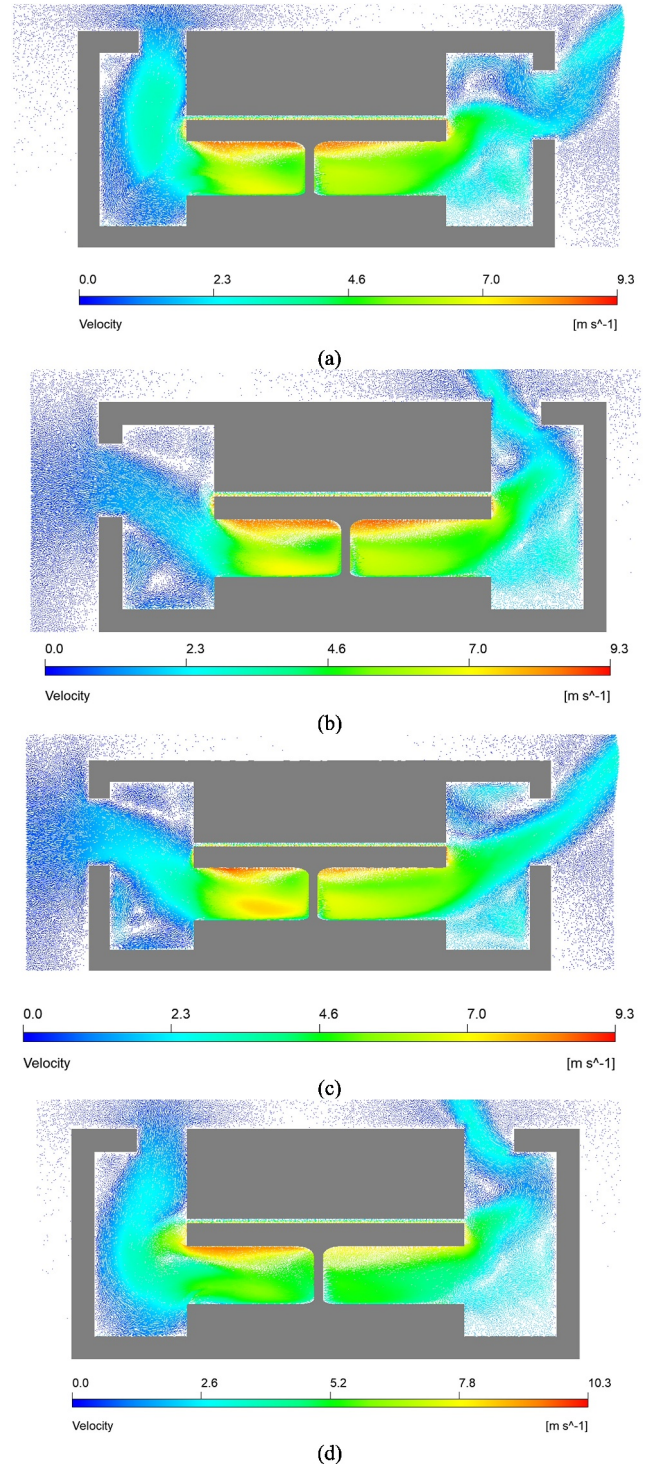
It is worth noting that this paper also examined the shapes of the inlet and outlet. The study found that using curved edges (see Figure 14) for the inlet/outlet in the endcap significantly improves airflow efficiency, thereby enhancing the cooling effect. However, as the space constraint, detailed results and explanations are not included in this paper.

Figure 15 shows vector diagrams of air velocities for various designs, with inlets being positioned on the left and outlets on the right. In all four designs, air is drawn in from the inlet, passes through the rotor chambers and is expelled from the outlet. However, due to the different positions of the inlets and outlets, the maximum air velocities vary. The highest velocity, 9.66 m/s, occurs in design III, whereas the lowest velocities,



**FIGURE 14** | Different inlet/outlet designs. (a) Design I: radial inlet + axial outlet, (b) design II: axial inlet + radial outlet, (c) design III: axial inlet and outlet and (d) design IV: radial inlet and outlet. All inlets on the left and outlets on the right.

8.34 m/s and 8.35 m/s, are observed in designs II and IV, respectively. This suggests that axial inlets and outlets have superior air intake and exhaust capacities compared to their radial counterparts. In the CFX postprocessing, the mass flow rate monitored at the inlet on the housing and its arithmetic mean over the entire area is calculated. For example, for the design I, when the fan rotates at 3000 rpm (target speed), it can draw 1.12 L air in and out per second. Moreover, the pressure loss from inlet to outlet is 3.7 Pa.



**FIGURE 15** | Air velocity streamline distribution of different designs. (a) Design I, (b) design II, (c) design III and (d) design IV.

However, higher air velocity does not necessarily correlate with better cooling efficiency. For instance, comparing the velocity vectors in Figure 15a,c, both with axial outlets but different inlets, shows that although the airflow speed is lower in Figure 15a, its design allows cold air to circulate in the end-winding region before being drawn into the rotor. This extended circulation enables more thorough contact with the EW, stator core and rotor core near the EW region, potentially resulting in better cooling. Therefore, to accurately assess cooling efficiency, it is essential to examine the temperature distributions throughout the investigated designs.

The PM and EW peak temperatures for all designs are shown in Figure 16. Here, the totally enclosed housing has also been included as a reference. The 4 proposed designs with self-cooling capability achieve significantly better cooling effects compared to a totally enclosed machine. It is also found that the maximum PM temperature of design I is the highest amongst all the proposed designs, whereas the others maintain a temperature of around 100°C. The maximum temperatures of the EW for all four designs are quite similar, each being around 79°C. Comparatively, design III or design IV can be considered as the best options.

To explain the results shown in Figure 16, the temperature distributions within the investigated designs are shown in Figure 17. Here, only the totally enclosed housing and the design III are shown, as the other designs have similar characteristics as the design III. As the totally enclosed housing design has no connection between the machine interior and the external environment, its cooling relies solely on heat radiation and natural convection on the housing and endplates. This is why it has the highest temperature, located on the PM, reaching 224.8°C as shown in Figure 17a. Figure 17b depicts the design III, where cool air is drawn in from the axial inlet on the left and directly expelled through the axial outlet. The highest temperature in this setup is 97.4°C on the PM. Comparing these two designs, it is evident that the design III achieves much better cooling effect inside the machine.

## 4 | Experiment Validation

### 4.1 | Prototype Machines and Test Rig

To expedite the experiment preparation, an existing 12-slot stator (see Figure 18a) was used to verify the accuracy of the

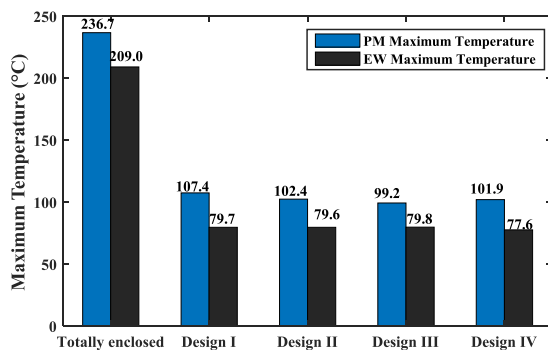


FIGURE 16 | Temperature comparison of different designs.

CFD simulation results, with its key parameters listed in Table 4. It is worth noting that the rated speed of the designed motor used in the CFD simulation is 3000 rpm. However, the prototype was tested at 400 rpm due to hardware limitations. The purpose of the experiment is to validate the self-cooling concept and the relative trends observed in simulation, particularly the airflow behaviour and thermal distribution, rather than to replicate the absolute temperatures at rated conditions.

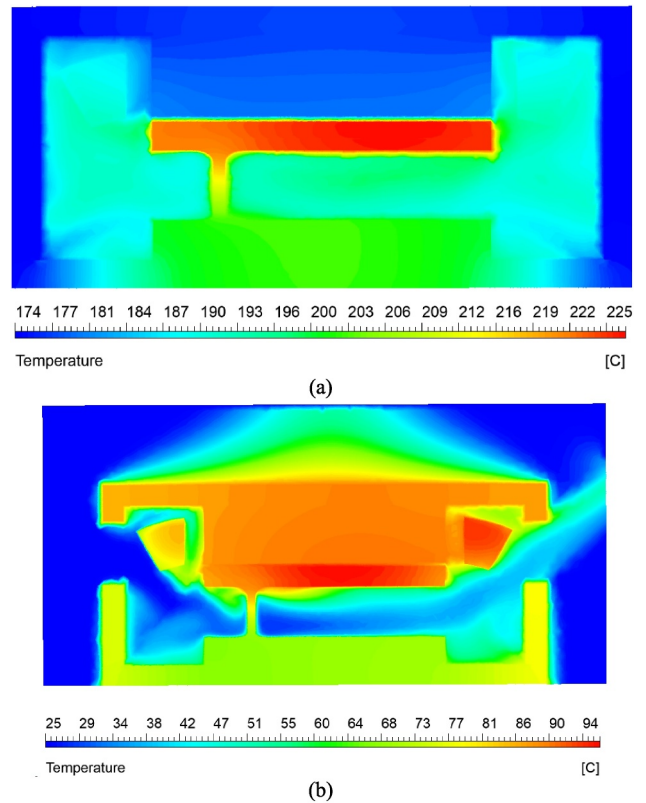


FIGURE 17 | Temperature contour of different designs. (a) Totally enclosed housing and (b) design III.

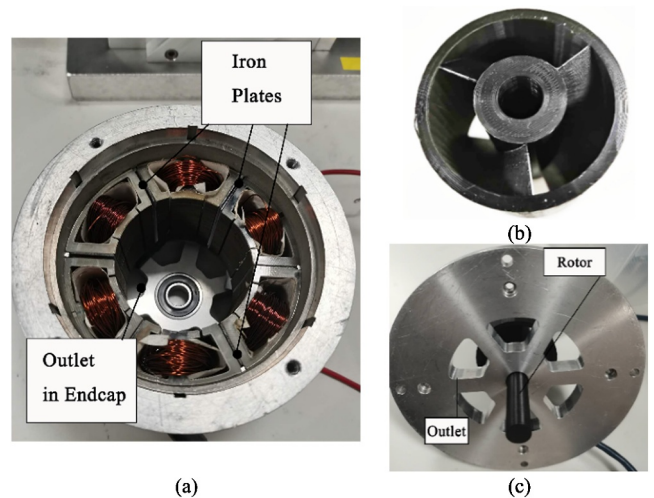


FIGURE 18 | 12-slot SPM prototype machine with self-cooling capability inner view. (a) Modular stator with housing, (b) 3D-printed 3-blade rotor without shaft and (c) outlet side endcap.



In addition, due to the complex blade structure, a 3D-printed plastic rotor without PMs was used as a substitute for the rotor core and PMs as shown in Figure 18b. Here, the rotor shaft has been removed to facilitate the observation of the blade structure. The 3D-printed rotor features a 2 mm thick 3-blade design. Additionally, to maintain the same airgap length, the outer and inner radii (blade radius) of the 3-D printed rotor were matched to those of the actual rotor with PMs. Figure 18c shows the one of the endcaps with outlets. The endcap with inlets is the same as the one shown in Figure 18c. It is worth noting that this setup was specifically designed to simplify the manufacturing of the integrated rotor blade structure. However, it still helps validate the accuracy of the CFD modelling and the effectiveness of the proposed self-cooling concept on the stator and EW regions, where most losses occur in the real machine. Due to the absence of PMs and thermal conductive rotor materials, the 3D-printed rotor does not generate heat and thus rotor temperature measurements were not relevant or meaningful in this specific context.

It is also worth noting that the existing stator has flux gaps in alternate stator teeth, resulting in a modular structure. A simple way to prevent the flux gaps in the modular stator from affecting the airflow is to use six iron plates inserted into these gaps to block the air passage as shown in Figure 18. Here, the iron plates were solely used to transfer heat between the modular stator segments and had no effect on the iron loss as the rotor is nonmagnetic. In addition, the heat source was solely generated by copper losses in the stator windings.

**TABLE 4** | Parameters of prototype modular SPM machine.

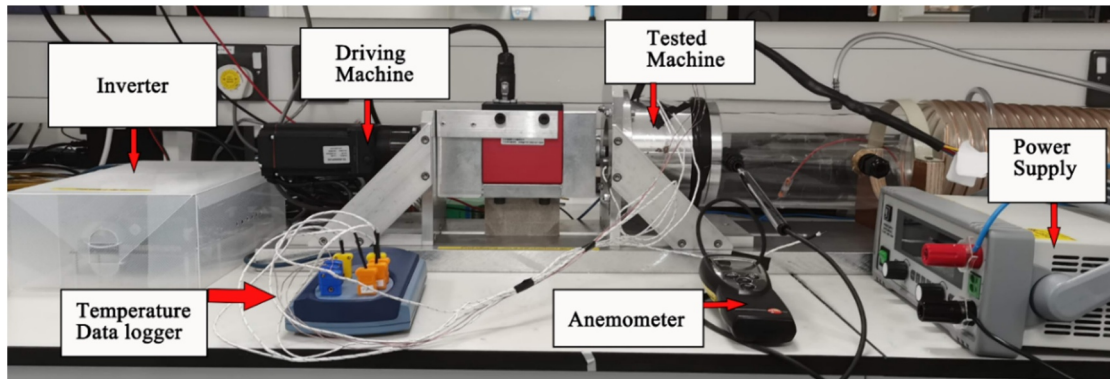
Slot number	12
Pole number	10
Stator outer radius (mm)	50
Stator inner radius (mm)	28.5
Airgap length (mm)	1
Rotor outer radius (mm)	27.5
Number of turns per coil	132
Stack length (mm)	50
Rated phase current (A)	7.34
Rated speed (rpm)	400

The complete test rig is shown in Figure 19. The prototype machine was driven by a dynamotor. To measure the temperatures at various parts of the prototype machine, six thermocouples were attached to the 3-phase active windings and EWs, that is, three for the active windings and three for the EWs. Additionally, some thermocouples were placed on the machine housing and in its surrounding environment to monitor the housing and the ambient temperatures, respectively. It is also noteworthy that the flow rate at the machine outlet was determined by measuring the average wind speed at the outlet using an anemometer and then multiplying it by the cross-sectional area of the outlet. The hot-wire anemometer assesses gas velocity by detecting variation in the electrical resistance of its heated wire, which changes with the passage of gas through it. Moreover, the temperatures of coils in the tested machines were monitored using T-type thermocouples, and the temperature was recorded by a data logger. The anemometer used in the experiment is testo 425—Thermo-anemometer with flow probe, and the thermocouples used are T-type with a temperature range of  $-270^{\circ}\text{C}$  to  $370^{\circ}\text{C}$ .

## 4.2 | Measured Results

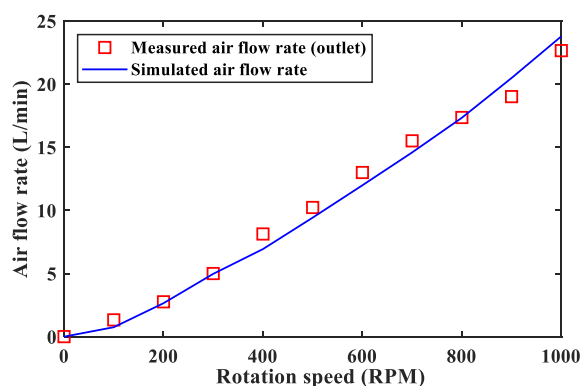
Figure 20 illustrates the relationship between the airflow rate at the outlet and rotor speed. The measurements were conducted at intervals of 100 rpm during the experiments. In general, the measured results match well with the simulation results, proving the accuracy of the 3D CFD models developed in this paper. The slight difference between the simulated and measured results might be due to the accuracy of the anemometer used. It is worth noting that the resolution limit of the instrument may cause uncertainty, the anemometer has a measurement accuracy of  $0.03 \text{ m/s} + 4.0\%$  of measured velocity for a speed range of 0.01 to  $+20 \text{ m/s}$ . As expected, when the rotation speed is 0 rpm, the airflow rate is 0 L/min. As the rotor speed increases, the airflow rate increases almost linearly, reaching 23.9 L/min at a speed of 1000 rpm.

Figure 21 shows the temperature variation of the EW and active coil with rotor speed. During the experiment, as three sets of thermocouples were placed on the EW and active coil of the machine's three phases, the average temperature across the three phases have been used. This is to avoid the impact of



**FIGURE 19** | Test rig for the machine with self-cooling capability.





**FIGURE 20** | Simulated and measured airflow rates versus rotor speed.

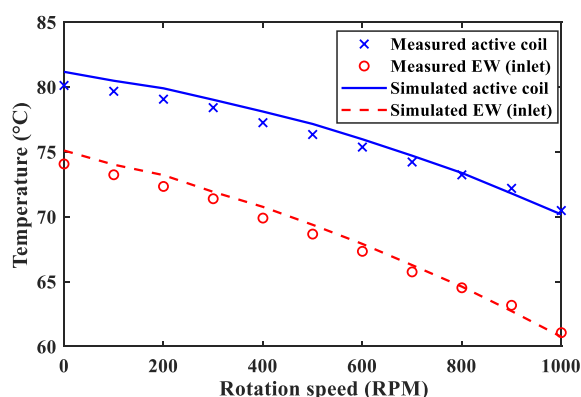


**FIGURE 21** | Simulated and measured temperatures versus rotor speed.

placement uncertainty of the thermal couples. The measured results indicate that the temperatures of both the EW and active winding decrease with increasing rotor speed, dropping from 74.1°C to 80.4°C and from 60.3°C to 72.0°C, respectively. The EW temperature is generally lower than that of the active coil because, compared to the active coil, this novel rotor design allows direct contact between cold air and the EW during rotation, resulting in more effective cooling of the EW section. The measured results confirm that, as anticipated, the blade rotor design enables the machine to achieve self-cooling capability.

## 5 | Conclusion

The paper introduces a self-cooling solution for SPM machines by adopting fan-blade shaped rotor core. To investigate its cooling effectiveness, 3D CFD models were established for simulations under various operating conditions such as different rotational speeds. The results indicate that this solution significantly improves the cooling of both the EW and PM by comparing to the baseline external fan-cooled machine. The study carefully examines the influence of the rotor blade height and the number of blades in the rotor structure (ranging from 1 to 7) and compares the temperatures of the EW and PM at the same rotational speed with different blade counts. The results show that 12 mm height of rotor blade is the most suitable for

self-cooling effect on PM and EW. Besides, although increasing the number of blades can lower the temperature of the PM, it also reduces the airflow intake, thus decreasing the cooling effectiveness for the EW. As a compromise, the paper recommends using a rotor structure with 3 blades.

Additionally, the paper has investigated the positions of the inlets and outlets on the housing and end-cap. To achieve better cooling for the EW, axial or radial inlets/outlets directly above and in front of the EW were used. The cooling effectiveness of four different inlet/outlet configurations was compared. Although the temperature differences in the EW among these configurations were minimal ( $< 3^{\circ}\text{C}$ ), there were significant differences in the cooling effectiveness for the PM. Among these, the axial inlet configuration resulted in the lowest PM temperature, and it was found that the choice of outlet had little impact on the temperature. Therefore, the paper suggests using an axial inlet, whereas the outlet choice can be flexible. The simulations and conclusions in this paper have been validated by tests.

In summary, the self-cooling capability in SPM machines enables efficient cooling performance without the need for additional space to accommodate rotor-mounted fans or air pumps. This feature makes the proposed structure particularly suitable for small to medium-sized SPM motors operating in the range of 1000–6000 rpm. Within this speed range, the self-cooling mechanism shows notable effectiveness, especially below 4000 rpm where the temperature reduction rate is more pronounced. Such motors can be utilised across a wide range of industrial applications, including domestic appliances, air compressors and electric vehicles, among others. However, it is also worth noting that, to prevent impurities from entering the air gap, dust covers and filters may need to be installed at the inlets and outlets. This is a common practice in devices, such as power tools and food blenders; therefore, no significant increase in manufacturing complexity is expected.

## Author Contributions

**Kaile Li:** writing – original draft. **Guang-jin Li:** supervision, writing – review and editing.

## Conflicts of Interest

The authors declare no conflicts of interest.

## Data Availability Statement

Data are available upon request due to privacy/ethical restrictions.

## References

1. Y. Chen, T. Cai, X. Zhu, D. Fan, and Q. Wang, "Analysis and Design of a New Type of Less-Rare-Earth Hybrid-Magnet Motor With Different Rotor Topologies," *IEEE Transactions on Applied Superconductivity* 30, no. 4 (2020): 1–6, <https://doi.org/10.1109/tasc.2020.2965879>.
2. N. Bianchi, E. Fornasiero, and W. Soong, "Selection of PM Flux Linkage for Maximum Low-Speed Torque Rating in a PM-Assisted Synchronous Reluctance Machine," *IEEE Transactions on Industry Applications* 51, no. 5 (2015): 3600–3608, <https://doi.org/10.1109/tia.2015.2416236>.

3. A. G. Shewalkar, A. S. Dhoble, and V. P. Thawkar, "Review on Cooling Techniques and Analysis Methods of an Electric Vehicle Motor," *Journal of Thermal Analysis and Calorimetry* 149, no. 12 (2024): 5919–5947, <https://doi.org/10.1007/s10973-024-13091-x>.
4. W. Cao, B. C. Mecrow, G. J. Atkinson, J. W. Bennett, and D. J. Atkinson, "Overview of Electric Motor Technologies Used for More Electric Aircraft (MEA)," *IEEE Transactions on Industrial Electronics* 59, no. 9 (2012): 3523–3531.
5. M. Cheng, W. Hua, J. Zhang, and W. Zhao, "Overview of Stator-Permanent Magnet Brushless Machines," *IEEE Transactions on Industrial Electronics* 58, no. 11 (2011): 5087–5101, <https://doi.org/10.1109/tie.2011.2123853>.
6. Z. Q. Zhu and D. Howe, "Electrical Machines and Drives for Electric, Hybrid, and Fuel Cell Vehicles," *Proceedings of the IEEE* 95, no. 4 (2007): 746–765, <https://doi.org/10.1109/jproc.2006.892482>.
7. W. Le, M. Lin, K. Lin, L. Jia, and A. Yang, "Design and Analysis of a Rotor Air-Cooling Enhanced Method for Axial Flux Permanent Magnet Machine With Housing-Cooling," *IEEE Transactions on Energy Conversion* 38, no. 3 (2023): 2136–2145, <https://doi.org/10.1109/tec.2023.3265676>.
8. M. Polikarpova, P. Ponomarev, P. Lindh, et al., "Hybrid Cooling Method of Axial-Flux Permanent-Magnet Machines for Vehicle Applications," *IEEE Transactions on Industrial Electronics* 62, no. 12 (2015): 7382–7390, <https://doi.org/10.1109/tie.2015.2465354>.
9. W. Geng, T. Zhu, Q. Li, and Z. Zhang, "Windings Indirect Liquid Cooling Method for a Compact Outer-Rotor PM Starter/Generator With Concentrated Windings," *IEEE Transactions on Energy Conversion* 36, no. 4 (2021): 3282–3293, <https://doi.org/10.1109/tec.2021.3084507>.
10. V. Ruuskanen, J. Nerg, M. Niemelä, J. Pyrhönen, and H. Polinder, "Effect of Radial Cooling Ducts on the Electromagnetic Performance of the Permanent Magnet Synchronous Generators With Double Radial Forced Air Cooling for Direct-Driven Wind Turbines," *IEEE Transactions on Magnetics* 49, no. 6 (2013): 2974–2981, <https://doi.org/10.1109/tmag.2013.2238679>.
11. F. Zhang, D. Gerada, Z. Xu, et al., "Improved Thermal Modeling and Experimental Validation of Oil-Flooded High-Performance Machines With Slot-Channel Cooling," *IEEE Transactions on Transportation Electrification* 8, no. 1 (2022): 312–324, <https://doi.org/10.1109/tte.2021.3106819>.
12. P. Liang, F. Chai, K. Shen, and W. Liu, "Water Jacket and Slot Optimization of a Water-Cooling Permanent Magnet Synchronous In-Wheel Motor," *IEEE Transactions on Industry Applications* 57, no. 3 (2021): 2431–2439, <https://doi.org/10.1109/tia.2021.3064779>.
13. W. Zhang, G. J. Li, B. Ren, Y. C. Chong, and M. Michon, "Investigation of Ferrofluid Cooling for High Power Density Permanent Magnet Machines," *IEEE Transactions on Magnetics* 59, no. 1 (2023): 1–11, <https://doi.org/10.1109/tmag.2022.3224787>.
14. L. Zhang, J. Paddock, G. Nellis, and B. Sarlioglu, "Novel Blade-Shaped Rotor Hub Design for Electric Machine Cooling," in *2023 IEEE Energy Conversion Congress and Exposition (ECCE)*, (2023), 4479–4486.
15. H. Ding, W. Sixel, L. Zhang, et al., "Evaluation of the Self-Cooling Performance of a Flux-Switching Permanent Magnet Machine With Airfoil-Shaped Rotor," *IEEE Transactions on Industry Applications* 57, no. 4 (2021): 3710–3721, <https://doi.org/10.1109/tia.2021.3083242>.
16. H. Shi, Q. Chen, J. Liao, Y. Zhou, G. Xu, and G. Liu, "Design and Optimization of Dual-Air Duct Cooling System for Rotor Permanent Magnet Flux-Switching Motor," *IEEE Transactions on Transportation Electrification* (2024): 1.
17. P. Lindh, I. Petrov, J. Pyrhönen, E. Scherman, M. Niemelä, and P. Immonen, "Direct Liquid Cooling Method Verified With a Permanent-Magnet Traction Motor in a Bus," *IEEE Transactions on Industry Applications* 55, no. 4 (2019): 4183–4191, <https://doi.org/10.1109/tia.2019.2908801>.
18. H. Luo, Y. Zhang, H. Wang, G. Liu, and F. Zhang, "Cooling Structure Design of High-Speed Permanent Magnet Synchronous Machine With Axial Ventilation Self-Cooling Rotor," *IEEE Access* 12 (2024): 27005–27016, <https://doi.org/10.1109/access.2024.3352608>.
19. Y. Kai and F. Yaojing, "Design of Novel Spiral Magnetic Poles and Axial-Cooling Structure of Outer-Rotor PM Torque Motor," *IEEE Transactions on Applied Superconductivity* 20, no. 3 (2010): 838–841.
20. K. M. Almohammadi, D. B. Ingham, L. Ma, and M. Pourkashanian, "2-D-CFD Analysis of the Effect of Trailing Edge Shape on the Performance of a Straight-Blade Vertical Axis Wind Turbine," *IEEE Transactions on Sustainable Energy* 6, no. 1 (2015): 228–235, <https://doi.org/10.1109/tste.2014.2365474>.
21. A. K. Lidtke, S. R. Turnock, and J. Downes, "Hydrodynamic Design of Underwater Gliders Using k-k L- $\omega$  Reynolds Averaged Navier-Stokes Transition Model," *IEEE Journal of Oceanic Engineering* 43, no. 2 (2018): 356–368.
22. W. R. Smith, "Modulation Equations and Reynolds Averaging for Finite-Amplitude Non-Linear Waves in an Incompressible Fluid," *IMA Journal of Applied Mathematics* 72, no. 6 (2007): 923–945, <https://doi.org/10.1093/imat/hxm054>.
23. N. V. Korovkin, D. Verkhovtsev, and S. Gulay, "Rotor Air-Cooling Efficiency of Powerful Turbogenerator," *IEEE Transactions on Energy Conversion* 36, no. 3 (2021): 1983–1990, <https://doi.org/10.1109/tec.2020.3045063>.
24. B. Wang, Y. Guo, O. Liu, and M. Shen, "Higher Order Accurate and High-Resolution Implicit Upwind Finite Volume Scheme for Solving Euler/Reynolds-Averaged Navier-Stokes Equations," *Tsinghua Science and Technology* 5, no. 1 (2000): 47–53.
25. N. Simpson, R. Wrobel, and P. H. Mellor, "Estimation of Equivalent Thermal Parameters of Impregnated Electrical Windings," *IEEE Transactions on Industry Applications* 49, no. 6 (2013): 2505–2515, <https://doi.org/10.1109/tia.2013.2263271>.
26. K. Kiyota, T. Kakishima, A. Chiba, and M. A. Rahman, "Cylindrical Rotor Design for Acoustic Noise and Windage Loss Reduction in Switched Reluctance Motor for HEV Applications," *IEEE Transactions on Industry Applications* 52, no. 1 (2016): 154–162, <https://doi.org/10.1109/tia.2015.2466558>.
27. S. H. Won, J. Choi, and J. Lee, "Windage Loss Reduction of High-Speed SRM Using Rotor Magnetic Saturation," *IEEE Transactions on Magnetics* 44, no. 11 (2008): 4147–4150, <https://doi.org/10.1109/tmag.2008.2001660>.
28. R. Wrobel, G. Vainel, C. Copeland, T. Duda, D. Staton, and P. H. Mellor, "Investigation of Mechanical Loss Components and Heat Transfer in an Axial-Flux PM Machine," *IEEE Transactions on Industry Applications* 51, no. 4 (2015): 3000–3011, <https://doi.org/10.1109/tia.2015.2405499>.
29. X. Wu, R. Wrobel, P. H. Mellor, and C. Zhang, "A Computationally Efficient PM Power Loss Mapping for Brushless AC PM Machines With Surface-Mounted PM Rotor Construction," *IEEE Transactions on Industrial Electronics* 62, no. 12 (2015): 7391–7401, <https://doi.org/10.1109/tie.2015.2455062>.
30. Y. Hu, S. Zhu, and C. Liu, "Magnet Eddy-Current Loss Analysis of Interior PM Machines for Electric Vehicle Application," *IEEE Transactions on Magnetics* 53, no. 11 (2017): 1–4, <https://doi.org/10.1109/tmag.2017.2700850>.
31. Z. Wu, Z. Q. Zhu, and H. Zhan, "Comparative Analysis of Partitioned Stator Flux Reversal PM Machine and Magnetically Geared Machine Operating in Stator-PM and Rotor-PM Modes," *IEEE Transactions on Energy Conversion* 32, no. 3 (2017): 903–917, <https://doi.org/10.1109/tec.2017.2693028>.